



# Anodic Synthesis of TiO<sub>2</sub> Nanotubes Influence of Water Content and the Analysis of the Nano-Mechanical Application

V. Sivaprakash<sup>1</sup> · R. Narayanan<sup>1</sup>

Received: 4 April 2020 / Revised: 22 July 2020 / Accepted: 23 July 2020 / Published online: 6 August 2020  
© Springer Nature Switzerland AG 2020

## Abstract

In terms of mechanical, chemical, and corrosion properties, the current research investigates the effect of nanotube's length by increasing the water content on the electrolyte. Self-assembled titanium dioxide (TiO<sub>2</sub>) nanotube was synthesized by electrochemical anodization using a neutral medium of ethylene glycol and ammonium fluoride. The experiments were carried out with two different water vol%. Subsequently, crystalline phases were achieved by annealing the sample at 550 °C. A scanning electron microscope confirmed that an increase in water content elevates the length of nanotube by three times than under normal conditions. The results demonstrate that the increased length of nanotube thus attained enhanced corrosion resistance and mechanical properties.

**Keywords** Anodization · TiO<sub>2</sub> nanotubes · Nanoindentation · Surface wettability · Corrosion

## 1 Introduction

Nowadays, titanium (Ti) and titanium alloy-based materials are highly preferred due to their widespread properties in different applications. Ti with its lightweight and high strength properties are one of the most sought materials for various applications in aerospace, biomedical, solar, and energy storage sectors [1]. Based on the biomedical application, Ti is highly recommended for its biodegradable and non-toxic nature. In general, materials that are non-modified or un-treated are avoided due to the release of toxic elements into the biological environment. Surface modification of Ti is usually performed in biomedical applications. Different surface modification techniques available are sol-gel, template synthesis, hydrothermal, physical vapor deposition, chemical vapor deposition, electrochemical, etc. [2–5]. Electrochemical anodization is one of the processes used to modify the surface more easily. The electrochemical anodization technique generally follows the sources of input voltage, anodization time, and fluoride ion present in the electrolyte [6, 7]. An increase in input potential (V), increase in anodization time are significant to increase the

length of nanotubes [8]. The influence of anodizing voltage and time has the functional property to change the thickness of TiO<sub>2</sub> nanotube. Different levels of water content and fluoride (NH<sub>4</sub>F) were analyzed for 1–14 h of anodization and an improvement in coating thickness was reported due to an increase in water content [9]. An increase or decrease in water content in the electrolytes can increase the length of nanotubes.

Without water content in the electrolyte, the oxygen atoms are highly bound with the carbon atoms so the dissolution process gets delayed, therefore, the addition of water helps to improve the growth of NTs [10]. Two-step of anodization was carried out and reported that fabricated nanotube on titanium and removed by sonication and its regrowth affect the bandgap energy [11]. The results of the initial anodization process demonstrate favoring the growth of nanotubes. The material containing ethylene glycol and ammonium fluoride were anodized for 24 h at 5 and 10 V and the different phase structures obtained have been analyzed [12]. The annealing process in general helps to change the material phases such as anatase, rutile, and brookite [12–14]. Reports on the influence of anodization voltage on the surface wettability properties owing to the different chemical compositions are also available [14, 15].

It has been reported that using 2 vol% of water content, 48 h of anodization, nanotubes as long as 8.5 μm (approximately) can be achieved [16], and also using the electrochemical

✉ R. Narayanan  
narayanan.ramaswamy@vit.ac.in

<sup>1</sup> School of Mechanical Engineering, VIT, Chennai, Tamil Nadu 600127, India

voltage ramp at 2 vol% of water, 500 nm nanotubes can be achieved [17]. It is interesting to observe that different electrolytes influence the geometrical parameters such as length and diameter, which affect the hydrophilic properties [14, 18].

Concerning biomedical applications, the deposition of calcium phosphate on TiO<sub>2</sub> nanotubes has proven to increase the corrosion resistance [19]. Synthesis of TiO<sub>2</sub> nanotubes with hydroxyapatite formations is advantageous in biomedical applications [19, 20]. Reports on different kinds of surfaces like unmodified Ti, nanotubes either crystalline, amorphous, or rutile are compared with cell culture container and has shown that the nanotube surface-modified titanium gives better results [21]. For the enhanced cell, viability and growth rate are the reason the nanotubes are encouraged in biomedical applications [22].

Studies on the synthesis of TiO<sub>2</sub> nanotubes by electrochemical anodization have been reported over the past 15 years. Though many are under investigation on the nanotubes, very few works have been reported on the influence of electrolyte water percentages [23–25]. The present work investigates the impact of electrolyte water content by evaluating the length of the nanotube and the mechanical, physical, and chemical properties of TiO<sub>2</sub> nanotubes. The results indicate that an increase in crystallinity and the length of the nanotube helps to improve the mechanical and physical behavior and thus improve its material performance.

## 2 Materials and Methods

Fabrication of TiO<sub>2</sub> nanotubes was carried out with two varying input potentials, i.e., 30 and 50 V and two different water contents (2.5 and 5 vol%) shown in Table 1. All the anodization was carried out for 1 h at room temperature (36 ± 2 °C). Before the anodization, all the samples were manually polished with 400–2000 microgrid (Si) sandpapers. After the polish, samples were chemically etched by 1:4:5 ratio of hydrofluoric acid, nitric acid, and water content present in the chemical etchant. Then the samples were dried with hydrogen-air to eliminate the moisture. Samples were annealed at 550 °C (± 5 °C) were applied to all the samples using a furnace. The Hitachi S-4800 scanning electron microscope was used to analyze the surface morphologies. Nanoindentation was performed using TI-900. BRUKER RFS 27 was used for the FT-Raman analysis. The contact angle was measured using a 4 μL (volume water) contact angle system (DSA100). Corrosion analysis was measured under the gamry instrument interface

**Table 1** Experimental condition of sample preparation

Sl. no.	Sample 1	Sample 2	Sample 3	Sample 4
Input voltage (V)	30	30	50	50
Water vol%	2.5	5	2.5	5

1010. All the corrosion analysis was performed under fresh simulated body fluid (SBF) solution. Preparation of SBF was prepared using NaCl 7.99 g, NaHCO<sub>3</sub> 0.350 g, KCl 0.224 g, K<sub>2</sub>HPO<sub>4</sub>·3H<sub>2</sub>O 0.228 g, MgCl<sub>2</sub>·H<sub>2</sub>O 0.305 g, 1 M HCL, CaCl<sub>2</sub> 0.278 g, Na<sub>2</sub>SO<sub>4</sub> 0.071 g.

## 3 Results and Discussion

### 3.1 Phase Analysis

The post-annealed samples were examined using X-ray diffraction at (condition of experiments). Anodized samples were subjected to heat treatment at 550 °C for 1 h. Sample 1 with an anodization condition of 30 V and 2.5 vol% water content during phase transformation exhibited a low level of crystallinity. Sample 2 at 550 °C delivered a phase transformation to crystallinity [26]. Sample 3, after the annealing process, underwent the highest phase transformation process as observed in the analysis. Sample 4 showed a change of phase structure. The intensity of peak rise at 25.8°, 38.6°, 40.5°, 48.5°, 53.0°, 62.3°, 70.7°, and the corresponding identified phases are noted in Fig. 1. The phase transformations started from the initial sample but the highest water content and input potential exhibited high crystallinity phase changes.

### 3.2 Surface Analysis

Figure 2 shows the fabricated samples of TiO<sub>2</sub> nanotubes analyzed by high-resolution scanning electron microscope (HR-SEM). The formation of nanotube in the presence of ethylene glycol and fluoride as an electrolyte delivered a

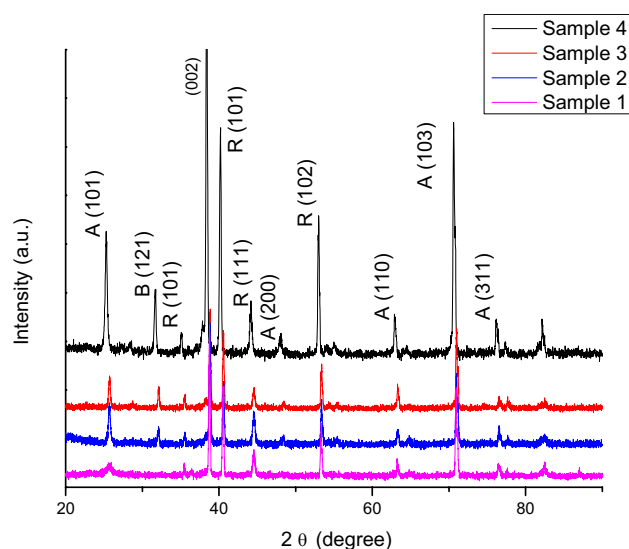


**Fig. 1** X-ray diffraction of TiO<sub>2</sub> nanotubes annealed at 550 °C

smooth and cylindrical shape. However, the presence of water in the structure of the nanotube made it rough and witnessed rib formation. The length of the nanotube obtained was 1.5  $\mu\text{m}$  as shown in Fig. 2a. The top view of  $\text{TiO}_2$  nanotubes shown in Fig. 2b indicates that nanotubes were equally distributed in the diameter range of 85–90 nm. When the water content increased to 5 vol%, the length of the nanotube (2.3  $\mu\text{m}$ ) increased as indicated by the cross-sectional view of nanotubes in Fig. 2c. In Fig. 2d, the nanotube top section shows the presence of debris and is clogged in the open side of the nanotubes. Upon an additional increase in input potential to 50 V, the nanotube growth increased leading to 5.35  $\mu\text{m}$  while using 2.5 vol% water content. The cross-sectional image (shown in Fig. 2e) indicates that an increase in input voltage reduces the rib structure formation and the tube diameter (shown in Fig. 2f).

The debris structure and clogged composition reduced with an increase in input voltage. Moreover, when the water

content increased to 5 vol%, the length of nanotube further increased to 6.8  $\mu\text{m}$  length as shown in Fig. 2g. By increasing the voltage and water content the sample surface structure showed low debris at the open end of nanotubes as shown in Fig. 2h. With 7 wt% of water involved in the electrolyte, a nanotube of 0.85  $\mu\text{m}$  (approx.) length was obtained [27]. Jianshou Kong et al. reported that a nanotube of 1.4  $\mu\text{m}$  length was acquired with 3 wt% of water content and with a different input potential [28].

### 3.3 Nanoindentation Test

The mechanical behavior of the material was evaluated using the nanoindentation test. Fabricated  $\text{TiO}_2$  nanotubes were cleaned with ethanol and dried using the nitrogen air. After polishing, the samples were placed in a table with caution that even a thumb impression could lead to changes in the material nanoindentation test results. The Berkovich

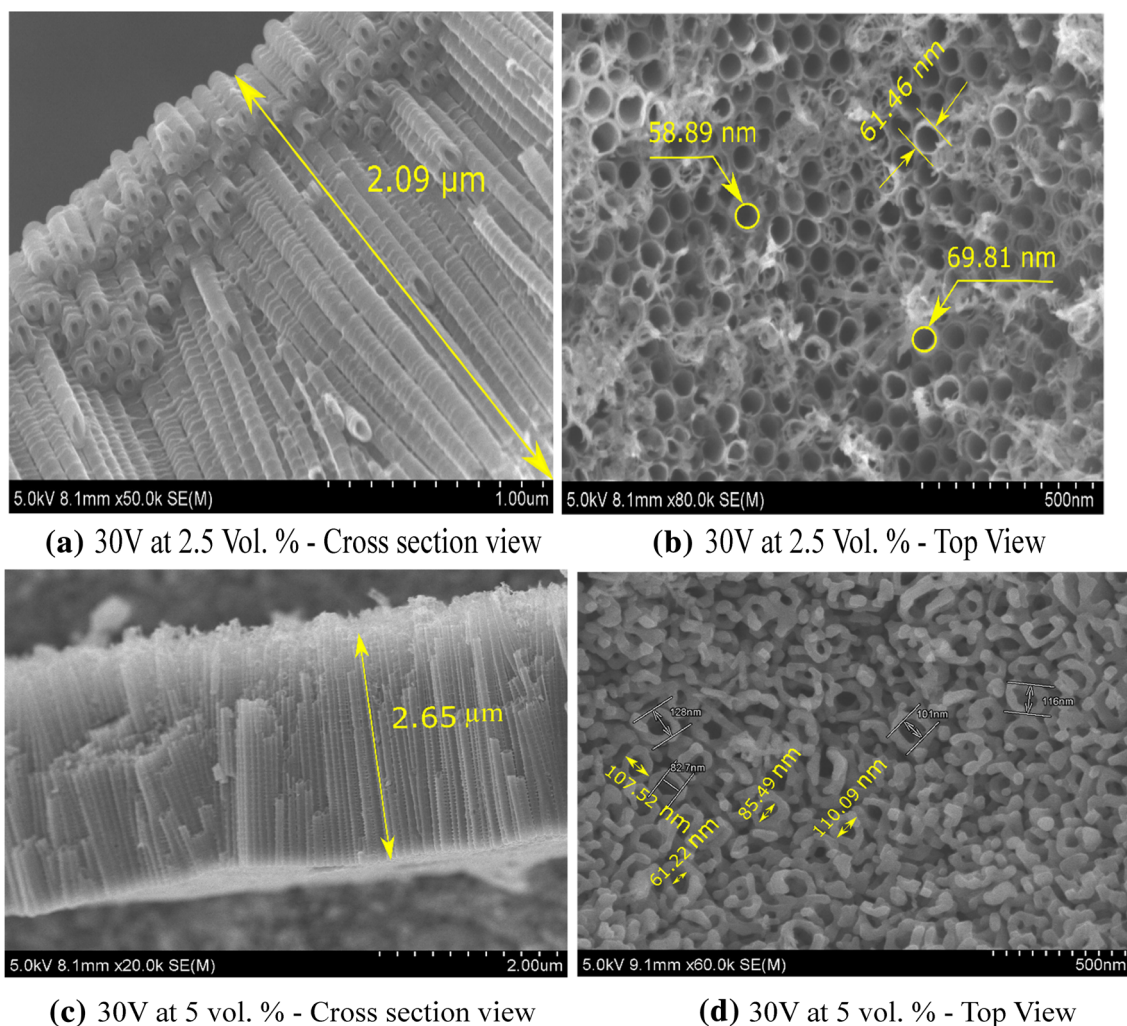


Fig. 2 Anodized  $\text{TiO}_2$  nanotubes



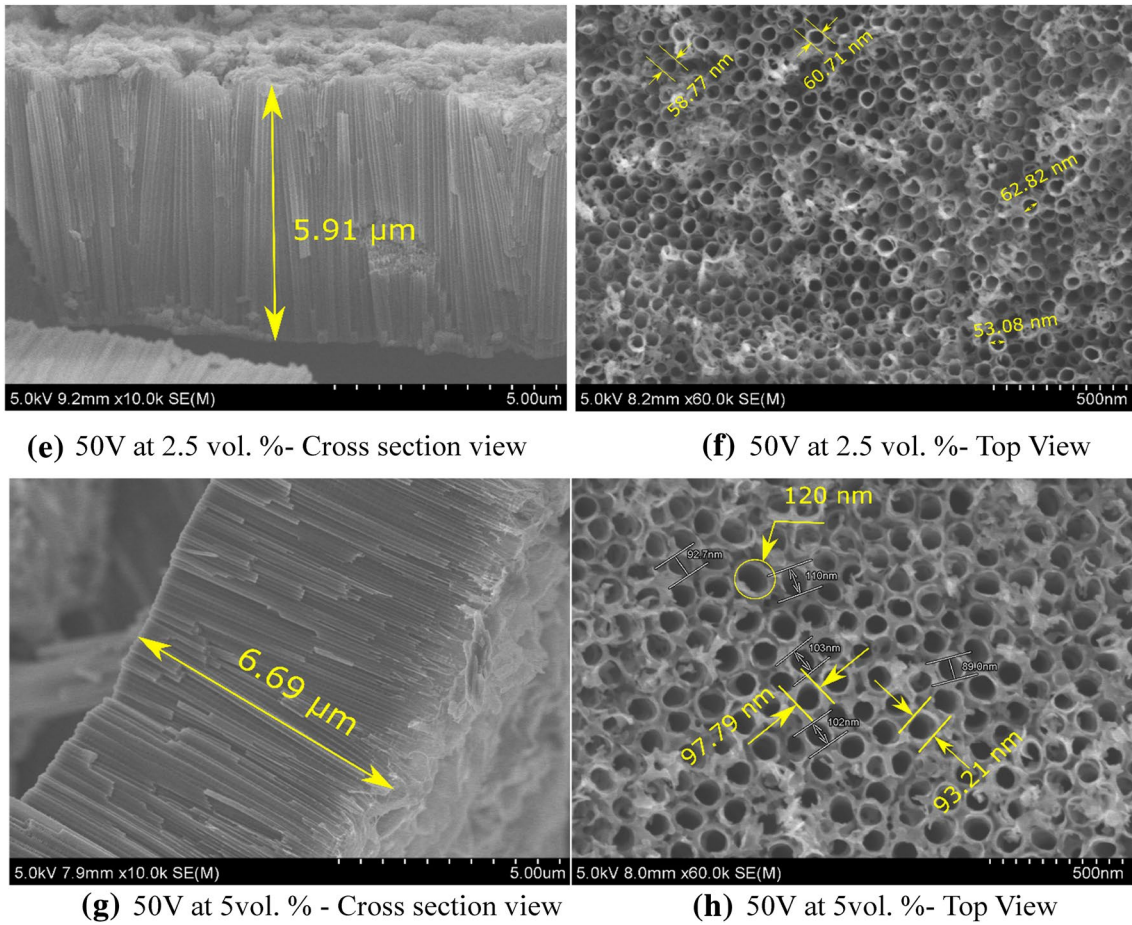


Fig. 2 (continued)

indenter was used to analyze the nano hardness. The load versus displacement chart is shown in Fig. 3. It can be noticed that the indentation and hardness values differed for every sample. A maximum load of 9 μN was used to identify the hardness of the nanotube. The initial portion of no-load starting from (1') was increased continuously to reach the maximum load (2')  $p_{max}$  at a constant loading condition of 50 mN/s. After reaching the maximum load, it was held for a few seconds ((2')–(3')). Then the load was released at the same load rate (4'). In this, the section of unloading helped in determining the material's elastoplasticity (critical stress existence), and plastic deformation. The values of nanoindentation are shown in Table 2. The penetration of indenter in the material or nanotube was identified and the maximum load displacements were analyzed.  $H$  refers to the hardness of the material by nanoindentation

$$H = \frac{P_{max}}{A} \tag{1}$$

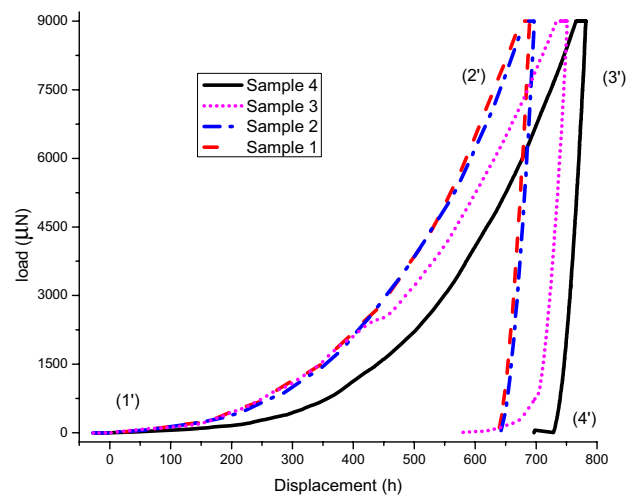


Fig. 3 Load vs. displacement nanoindentation

**Table 2** Nanoindentation hardness (load vs displacement) and contact angle measurement

Samples	Contact depth	Max. indentation force	Unloading curve slope	Contact area	Max. penetrating depth	Elastic modulus of tips	Contact angle (°)
	$H_c$ (nm)	$P_{max}$ (μN)	$S$ (μN/nm)	$A$ (nm <sup>2</sup> )	$H_{max}$ (nm)	$E_r$ (GPa)	
Sample 1	664.4577	8998.732	265.7275	11,197,137	690.7343	70.3587	15.59
Sample 2	671.0665	8999.192	257.5965	11,408,377	697.0033	67.5714	86.36
Sample 3	725.3724	8998.949	258.5171	13,221,142	751.3568	62.99261	33.19
Sample 4	757.658	8997.632	278.652	14,364,071	781.7685	65.14157	31.19

$P_{max}$  denotes the maximum load applied to the material,  $A$  identified for the maximum contact between the indenter and the material area. The area of surface contact to the sample is calculated using Eq. 2

$$A = 3\sqrt{3h_f^2 \tan^2 65.3} = 23.96h_f^2 \quad (2)$$

The contact indentation is identified by the following equation (Eq. 3)

$$h_f = h_{max} - \epsilon \frac{P_{max}}{S} \quad (3)$$

where  $S$  is known as the stiffness coefficient of the unload indentation  $3^{-4}$ . In this unloading, the condition could be observed by the material's plasticity and elasticity condition [29, 30]. The material maximum unloading point could be calculated using Eq. 4

$$S = \left( \frac{\partial p}{\partial h} \right)_{h=h_{max}} \quad (4)$$

The values of loading and unloading depend upon the nanotube's crystallinity. After the heat treatment, the crystalline sizes increased [31] and the increments were reflected in the strength of nanoindentation hardness.

Table 2 depicts the variation of contact depth from material to material due to the varying length of the nanotubes in different materials. When the nanotube's length increased, the penetration depth and the contact depth were increased, simultaneously. The maximum displacement was in the range of 751–781 nm. Moreover, the maximum peak intensity took place in sample 4 at 550 °C and the hardness values for the annealed sample were comparatively the same in previous values [32].

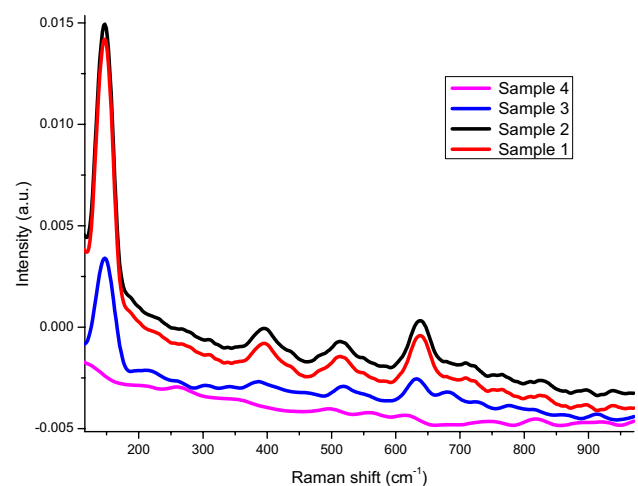
### 3.4 Raman Shift Analysis

Raman spectroscopy was used to identify the phase composition and surface homogeneity. Figure 4 shows the Raman spectrum for plain and samples 1, 3, 4 using 514 nm laser lines.

The Raman intensity shows anatase peaks appearing as four bands in 147, 398, 515, 636 cm<sup>-1</sup> ascribed to anatase assigned  $E_g$ ,  $B_{1g}$ ,  $A_{1g}/B_{1g}$ , and  $E_g$ , respectively. Group theory applied to molecular vibration uses notation for one dimension as  $A$  or  $B$  (non-degenerate mode), two dimensions as  $E$  (double degenerate), three dimensions as  $T$  (triple degenerate) and the subscription number 1 or 2 represent the symmetric and non-symmetric principle symmetric axis. The final subscription of  $g$  or  $u$  refers to the symmetric or anti-symmetric refer to the inversion of coordinates. Chen et al. reported on multi-wall carbon nanotube (MWCNT), a mixture of TiO<sub>2</sub>/MWCNT receives different spectrums in Raman shift, and they reported that improved surface area MWCNT improves the pH sensitivity [33]. Simultaneously, the maximum length nanotube nano hardness for sample 4 differs from the all balanced sample.

### 3.5 Surface Wettability Analysis

The surface wetting behavior of prepared samples was investigated from contact angle measurement shown in Fig. 5. The anodized sample length of 1.5, 2.3, 5.35, 6.8 μm, and the corresponding contact angle of the samples are shown in Table 2.

**Fig. 4** Raman spectra of TiO<sub>2</sub> nanotubes samples

The different lengths of nanotubes exhibited different wetting behaviors. Sample 2 had the highest contact angle due to subsurface nanotube that became rough after anodization, thus lead to a higher wettability material turned as hydrophilic. Alnough et al. reported the surface radius, chemical structure, flow dynamics, and interface interaction [34].

Zhang et al. suggested that small water contact angle materials deliver high cell viability and proliferation [19]. However, the increase in water content to 5 vol% increased the contact angle of the material and simultaneously with an increase in input potential, the material wetting behavior was reduced below  $35^\circ$  indicating that an increase in voltage may influence the surface wettability.

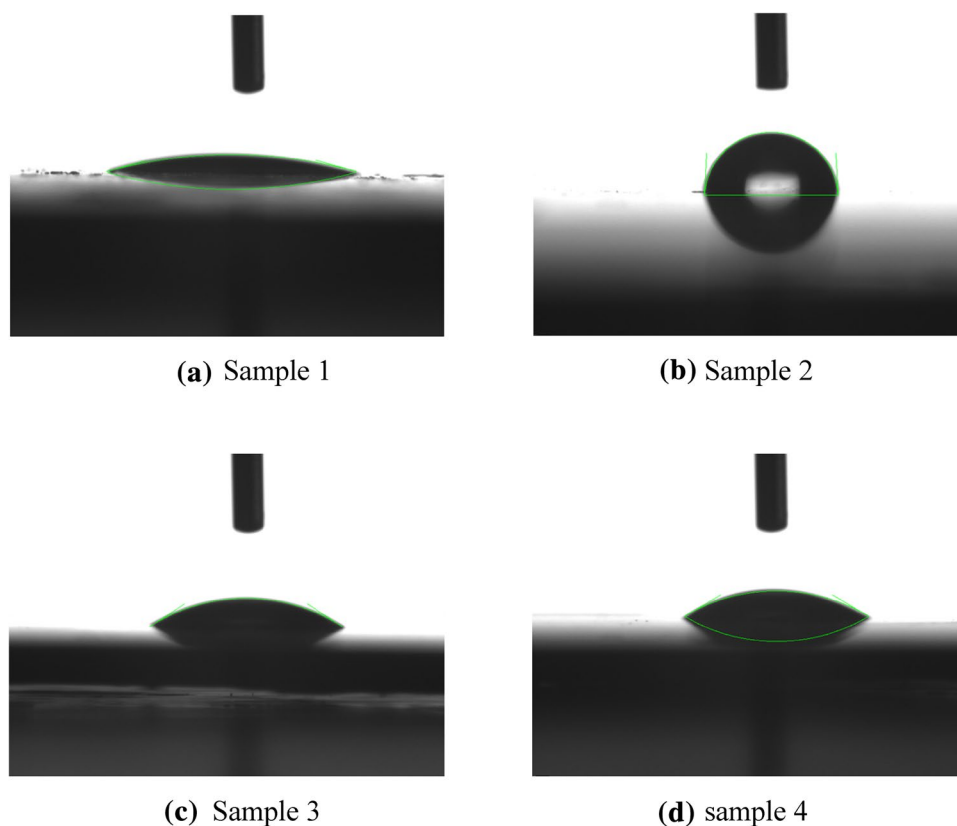
### 3.6 Corrosion Analysis

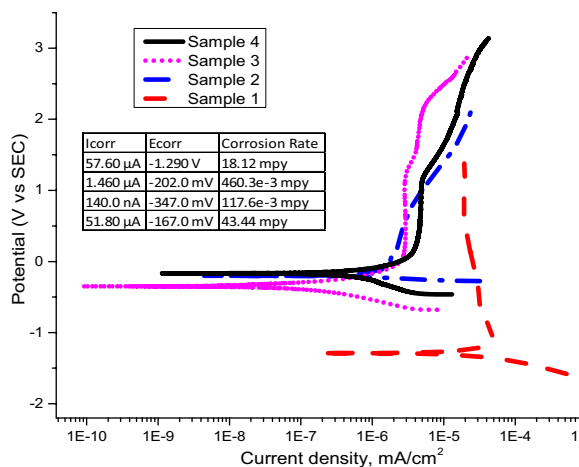
The role of the passive layer is to protect the material from the harmful chemical environment, improve acidic anticorrosion and primary environment. Figure 6a shows us the electrochemical polarization technique with anodized rapid input current zone characterized by computerized potentiostats. The device was connected with working sense anode as-fabricated end, counter electrode as platinum wire, and reference electrode as calomel saturated electrode. The working sample exposed area was  $1.0 \text{ cm}^2$ . The balance area

was sealed with adhesion tape. The SBF solution was used to characterize the corrosion analysis. The potentiodynamic polarization was initiated with  $-1500$  to  $2000 \text{ mV}$  with a scan rate of  $1 \text{ mV/s}$ . Before the polarization analysis, the sample was held for  $30 \text{ min}$  in the SBF solution for better corrosion results. The solution temperature was continuously monitored and every experiment was conducted with a fresh solution. The table in Fig. 6a shows the corrosion values measured from different  $\text{TiO}_2$  nanotubes. The secure passivation layer could lead to high corrosion resistance in the titanium oxide nanotubes with a length of  $1.5 \mu\text{m}$ . The water content of  $2.5 \text{ vol}\%$  of the corrosion current density  $i_{\text{corr}}$  result indicates that higher than  $5 \text{ vol}\%$  of water. Also, an increase in input potential level up to  $50 \text{ V}$ , the  $i_{\text{corr}}$  value delivered more positive benefits of  $140$  shown in the table. However, the final increase in water percentage the value comes down to the same as  $30 \text{ V } 2.5$  water percentage. Gradually, the corrosion potential ( $E_{\text{corr}}$ ) values shifted to positive values showing that with an increase in voltage and water content, the samples become more corrosion-resistant.

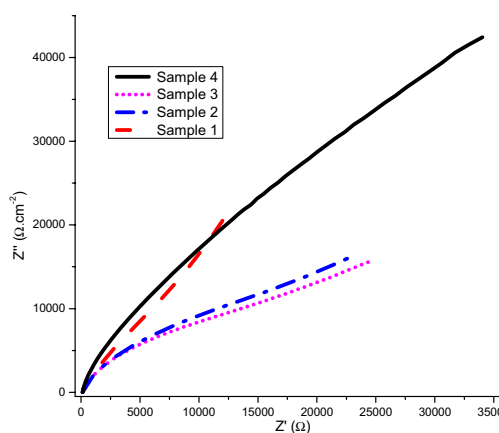
Reduction in anodic and cathodic curves indicate that current density ( $i_{\text{corr}}$ ) value reductions happen due to the increase in the length of nanotubes. The low corrosion rate and change in high corrosion rate were the reasons for crystallinity change after heat treatment. The peak intensity showed an increase relating to the crystallinity after

**Fig. 5** Surface wettability of different length anodized  $\text{TiO}_2$  nanotubes





(a) Potentiodynamic polarization curve obtained at different length of nanotubes.

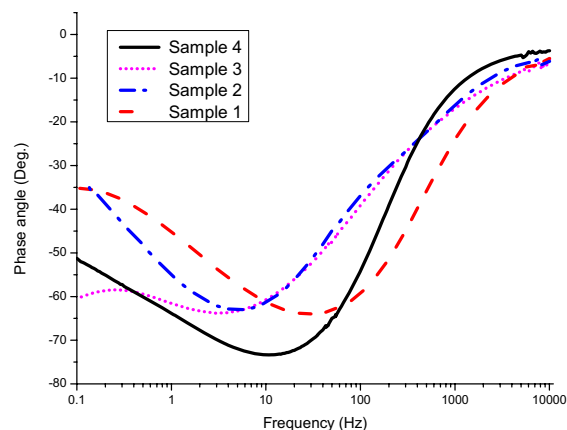


(b) The Nyquist plot in SBF

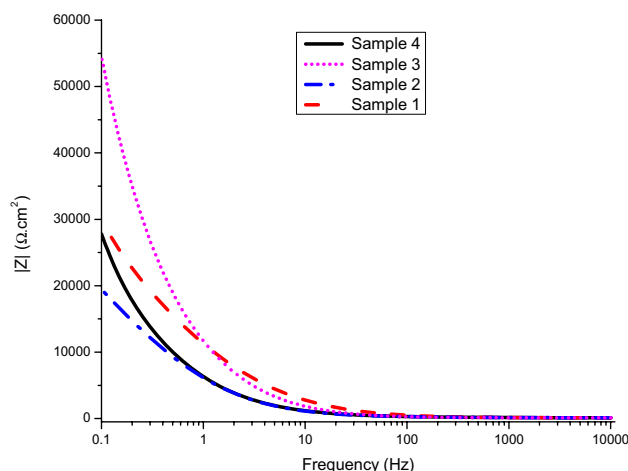
**Fig. 6** Potentiodynamic polarization of TiO<sub>2</sub> nanotubes and electrochemical impedance spectroscopy

550 °C of heat treatment. The maximum length of nanotubes sample under nano hardness testing, the deformation of nanoindenter may increase the corrosion resistance.

TiO<sub>2</sub> nanotubes were studied to characterize the electrochemical impedance and the impedance spectra fitted with an equivalent electrical circuit model using gamry instrument. This analysis evaluates the insulation property and structural defects. Figure 6b shows the Nyquist plot result obtained from the EIS analysis. The plot of samples 1, 2, 3, and 4 indicate the flow of the plot in a semi-circle shape. The semi-circled shape indicates the resistivity of material in the SBF solution. These plot results are represented by the equivalent electrical circuit and present three-time constant as shown in capacitive behavior, where  $R_s$  is the solution resistance,  $R_t$  denotes the charge transfer resistance,  $Q_{dl}$  is noted as double-layer constant phase element as shown in Fig. 7a, b. Table 3 shows the corresponding values of equivalent circuits.



(a) Frequency vs phase angle



(b) Frequency Vs. Magnitude

**Fig. 7** Bode plots in SBF solution

The TiO<sub>2</sub> nanotube porous layer changed to the electrochemical interface, as that circuit is shown in Fig. 8 and confirms the impedance changed in Fig. 7a, b bode plots. The electrochemical AC impedance EEC (an equivalent electrical circuit) is shown in Fig. 8. The polarization resistance values decreased due to the TiO<sub>2</sub> nanotubes coating invasion of the solution on nanotube surfaces. The penetration of SBF to the TiO<sub>2</sub> nanotubes takes a three-time constant in an equivalent electrical circuit. Figure 8 Model (a) shown as the plain smooth titanium immersed and was used to analyze the corrosion resistance. Model (b) represents titanium and the barrier layer while model (c) represents the titanium barrier layer and nanotubes. The result of resistance in nanotubes and coating resistance was due to the improvement in length of nanotubes and the crystallinity. The heat treatment process changed the material phases and that phase conversion improved the substantial corrosion resistance.

**Table 3** Parameters for an equivalent electrical circuit for TiO<sub>2</sub> nanotube fabricated samples

	$R_s$ ( $\Omega\cdot\text{cm}^2$ )	$R_2$ ( $\Omega\cdot\text{cm}^2$ )	$\text{CPE}_1$ ( $Q_3$ ) ( $S^*s^a$ )	$n_2$	$R_3$ ( $\Omega\cdot\text{cm}^2$ )	$\text{CPE}_2$ ( $Q_4$ ) ( $S^*s^a$ )	$n_3$	$\chi^2$
Sample 1	278.5	$2.498e^{-6}$	$815.5e^{-3}$	213.2	$19.33e^{-6}$	$848.1e^{-3}$	119.5	$496.6e^{-6}$
Sample 2	$13.39e^3$	$27.44e^{-6}$	$556.5e^{-3}$	123.7	$10.45e^{-6}$	$839.5e^{-3}$	$63.73e^3$	$345.5e^{-6}$
Sample 3	$15.74e^3$	$35.04e^{-6}$	$334.8e^{-3}$	125.9	$35.04e^{-6}$	$862.1e^{-3}$	$5.850e^3$	$129.7e^{-6}$
Sample 4	126	$22.21e^{-6}$	$920.5e^{-3}$	$8.142e^3$	$31.63e^{-6}$	$876.6e^{-3}$	$114.3e^3$	$353.1e^{-6}$

$s^a$  represents the non-uniform distribution

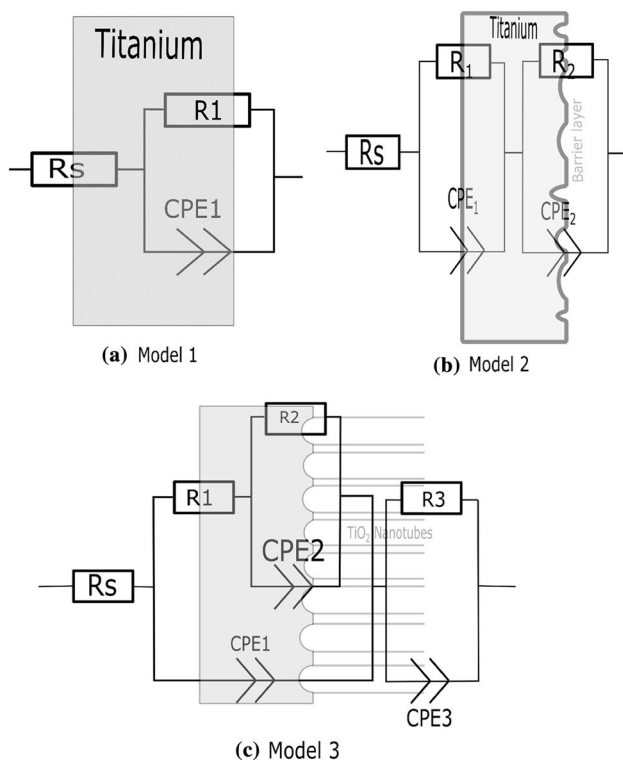


**Fig. 8** Models of the equivalent circuit from the EIS-results used for fitting electrochemical data

## 4 Conclusions

Fabrication of TiO<sub>2</sub> nanotubes by the electrochemical method using the anodization process with various water percentages was analyzed. XRD, HR-SEM, nanoindentation, Raman shift, contact angle measurement, and corrosion analysis were investigated. The annealing process led to a crystalline sharp anatase peak at 25.8° as confirmed by X-ray diffraction analysis. From the surface analysis using HR-SEM, the sample anodized at 50 V with 5 vol% of water presence in electrolyte delivered the maximum length of 6.8  $\mu\text{m}$  of nanotubes. The nanoindentation test revealed that mechanical property increased with an increase in the thickness of nanotubes. Raman spectral analysis helped in the identification of anatase phase-shifts

in  $E_g$ ,  $B_{1g}$ ,  $A_{1g}$ ,  $E_g$  peak intensities at 636  $\text{cm}^{-1}$  in samples 3 and 4. Surface wetting behavior analysis indicated that samples 3 and 4 achieved the maximum wetting behavior of 33.19° and 31.19° shows that the material gained super hydrophilicity behavior. The potentiodynamic polarization examination result indicated that a high passive range occurred in the high coating thickness layer under the SBF solution. The lowest  $i_{\text{corr}}$  value of 140 nA (sample 3) designated the best outcome among the other samples. The corrosion rate in samples 2 and 3 was lower compared to others.

From the above results, it may be concluded that the maximum length nanotube delivers the highest strength to the material. For applications in mechanical and biological sectors, sample 4 with conditions of 50 V and 5 vol% of water content is observed as the best among the other samples.

**Acknowledgments** We gratefully thank the VIT Chennai campus for providing the necessary facilities to complete this research work.

## Compliance with Ethical Standards

**Conflict of interest** There are no conflicts to declare.

## References

- Zhang LC, Chen LY (2019) A review on biomedical titanium alloys: recent progress and prospect. *Adv Eng Mater* 21:1–29. <https://doi.org/10.1002/adem.201801215>
- Indira K, Kamachi Mudali U, Rajendran N (2017) Development of self-assembled titania nanopore arrays for orthopedic applications. *J Bio Tribo Corros*. <https://doi.org/10.1007/s40735-016-0068-6>
- Parcharoen Y, Termsuksawad P, Sirivisoot S (2016) Improved bonding strength of hydroxyapatite on titanium dioxide nanotube arrays following alkaline pretreatment for orthopedic implants. *J Nanomater* 2016:1–13. <https://doi.org/10.1155/2016/9143969>
- Zhang K, Cao S, Li C et al (2019) Rapid growth of TiO<sub>2</sub> nanotubes under the compact oxide layer: evidence against the digging manner of dissolution reaction. *Electrochem Commun* 103:88–93. <https://doi.org/10.1016/j.elecom.2019.05.015>
- Zalnezhad E, Hamouda AMS, Faraji G, Shamshirband S (2015) TiO<sub>2</sub> nanotube coating on stainless steel 304 for biomedical applications. *Ceram Int* 41:2785–2793. <https://doi.org/10.1016/j.ceramint.2014.10.098>



6. Benčina M, Junkar I, Zaplotnik R et al (2019) Plasma-induced crystallization of TiO<sub>2</sub> nanotubes. *Materials (Basel)* 12:1–13. <https://doi.org/10.3390/ma12040626>
7. Saharudin KA, Sreekantan S, Mydin RBSNM, Basiron N, Krengvirat W (2018) Factor affecting geometry of TiO<sub>2</sub> nanotube arrays (TNAs) in aqueous and organic electrolyte. *Intech Open*. <https://doi.org/10.5772/intechopen.74193>
8. Adán C, Marugán J, Sánchez E et al (2016) Understanding the effect of morphology on the photocatalytic activity of TiO<sub>2</sub> nanotube array electrodes. *Electrochim Acta* 191:521–529. <https://doi.org/10.1016/j.electacta.2016.01.088>
9. Su Z, Zhang L, Jiang F, Hong M (2013) Formation of crystalline TiO<sub>2</sub> by anodic oxidation of titanium. *Prog Nat Sci Mater Int* 23:294–301. <https://doi.org/10.1016/j.pnsc.2013.04.004>
10. Lim YC, Zainal Z, Hussein MZ, Tan WT (2012) Effect of water content on structural and photoelectrochemical properties of titania nanotube synthesized in fluoride ethylene glycol electrolyte. *Adv Mater Res* 501:204–208. <https://doi.org/10.4028/www.scientific.net/AMR.501.204>
11. Pishkar N, Ghorannevis M, Ghorannevis Z, Akbari H (2018) Study of the highly ordered TiO<sub>2</sub> nanotubes physical properties prepared with two-step anodization. *Results Phys* 9:1246–1249. <https://doi.org/10.1016/j.rinp.2018.02.009>
12. Lucia A, Andres J, Chaves M et al (2016) Surface modification of the alloy Ti-7.5 Mo by anodization for biomedical applications. *Mater Sci Forum* 869:913–917. <https://doi.org/10.4028/www.scientific.net/MSF.869.913>
13. Preethi LK, Antony RP, Mathews T et al (2017) A study on doped heterojunctions in TiO<sub>2</sub> nanotubes: an efficient photocatalyst for solar water splitting. *Sci Rep* 7:1–15. <https://doi.org/10.1038/s41598-017-14463-0>
14. Liu G, Du K, Wang K (2016) Surface wettability of TiO<sub>2</sub> nanotube arrays prepared by electrochemical anodization. *Appl Surf Sci*. <https://doi.org/10.1016/j.apsusc.2016.01.010>
15. Han B, Nezhad EZ, Musharavati F et al (2018) Tribo-mechanical properties and corrosion behavior investigation of anodized Ti-V alloy. *Coatings* 8:1–22. <https://doi.org/10.3390/COATINGS8120459>
16. Xu YN, Liu MN, Wang MC et al (2015) Nanoindentation study of the mechanical behavior of TiO<sub>2</sub> nanotube arrays. *J Appl Phys*. <https://doi.org/10.1063/1.4932213>
17. Bilek O, Fohlerova Z, Hubalek J (2019) Enhanced antibacterial and anticancer properties of Se-NPs decorated TiO<sub>2</sub> nanotube film. *PLoS One* 14:1–15. <https://doi.org/10.1371/journal.pone.0214066>
18. Munirathinam B, Pydimukkala H, Ramaswamy N, Neelakantan L (2015) Influence of crystallite size and surface morphology on electrochemical properties of annealed TiO<sub>2</sub> nanotubes. *Appl Surf Sci* 355:1245–1253. <https://doi.org/10.1016/j.apsusc.2015.08.017>
19. Huang Y, Xu Z, Zhang X et al (2017) Nanotube-formed Ti substrates coated with silicate/silver co-doped hydroxyapatite as prospective materials for bone implants. *J Alloys Compd* 697:182–199. <https://doi.org/10.1016/j.jallcom.2016.12.139>
20. Ichim L, Dumitriu C, Surugiu A et al (2017) Elaboration and characterization of a complex coating on Ti with TiO<sub>2</sub> nanotubes, functionalized single carbon nanotubes, hydroxyapatite and iron. *Ann Acad Roman Sci Ser Phys Chem Sci* 2:1–7
21. Khrunyk YY, Belikov SV, Tsurkan MV et al (2020) Surface-dependent osteoblasts response to TiO<sub>2</sub> nanotubes of different crystallinity. *Nanomaterials* 10:1–17. <https://doi.org/10.3390/nano10020320>
22. Benčina M, Junkar I, Mavrič T et al (2019) Performance of annealed TiO<sub>2</sub> nanotubes in interactions with blood platelets. *Mater Tehnol* 53:791–795. <https://doi.org/10.17222/mit.2018.249>
23. Nesheva D, Babeva T, Vasileva M et al (2019) Phase characterization and ethanol adsorption in TiO<sub>2</sub> nanotubes anodically grown on Ti6Al4V alloy substrates. *J Alloys Compd* 798:394–402. <https://doi.org/10.1016/j.jallcom.2019.05.247>
24. Guan D, Hymel PJ, Wang Y (2012) Growth mechanism and morphology control of double-layer and bamboo-type TiO<sub>2</sub> nanotube arrays by anodic oxidation. *Electrochim Acta* 83:420–429. <https://doi.org/10.1016/j.electacta.2012.08.036>
25. Benčina M, Junkar I, Zaplotnik R, Valant M, Igljč A, Mozetič M (2019) Plasma-induced crystallization of TiO<sub>2</sub> nanotubes. *Materials* 626:1–13. <https://doi.org/10.3390/ma12040626>
26. Pérez DAG, Jorge Junior AM, Asato GH et al (2019) Surface anodization of the biphasic Ti13Nb13Zr biocompatible alloy: influence of phases on the formation of TiO<sub>2</sub> nanostructures. *J Alloys Compd* 796:93–102. <https://doi.org/10.1016/J.JALLCOM.2019.04.167>
27. Necula MG, Mazare A, Ion RN et al (2019) Lateral spacing of TiO<sub>2</sub> nanotubes modulates osteoblast behavior. *Materials (Basel)* 12:2956. <https://doi.org/10.3390/ma12182956>
28. Yu M, Cui H, Ai F et al (2018) Terminated nanotubes: evidence against the dissolution equilibrium theory. *Electrochem Commun* 86:80–84. <https://doi.org/10.1016/j.elecom.2017.11.025>
29. Mansour M, Tsongas K, Tzetzis D (2019) Measurement of the mechanical and dynamic properties of 3D printed polylactic acid reinforced with graphene. *Polym Technol Mater* 58:1234–1244. <https://doi.org/10.1080/03602559.2018.1542730>
30. Briscoe BJ, Fiori L, Pelillo E (1998) Nano-indentation of polymeric surfaces. *J Phys D Appl Phys* 31:2395–2405. <https://doi.org/10.1088/0022-3727/31/19/006>
31. Mercado CC, Lubrin MEL, Hernandez HAJ, Carubio RA (2019) Comparison of photoelectrochemical current in amorphous and crystalline anodized TiO<sub>2</sub> nanotube electrodes. *Int J Photoenergy*. <https://doi.org/10.1155/2019/9848740>
32. Barbana N, Ben Youssef A, Dhiflaoui H, Bousselmi L (2018) Preparation and characterization of photocatalytic TiO<sub>2</sub> films on functionalized stainless steel. *J Mater Sci* 53:3341–3363. <https://doi.org/10.1007/s10853-017-1755-5>
33. Chen Y, Mun SC, Kim J (2013) A wide range conductometric pH sensor made with titanium dioxide/multiwall carbon nanotube/cellulose hybrid nanocomposite. *IEEE Sens J* 13:4157–4162. <https://doi.org/10.1109/JSEN.2013.2261812>
34. Alnoush W, Sayed A, Alyafei N (2019) Optimization of contact angle and interfacial tension measurements for fluid/rock systems at ambient conditions. *MethodsX* 6:1706–1715. <https://doi.org/10.1016/j.mex.2019.07.009>

**Publisher's Note** Springer Nature remains neutral with regard to jurisdictional claims in published maps and institutional affiliations.